

## A comparative study of two constitutive models within an inverse approach to determine the spatial stiffness distribution in soft materials

Y. Mei<sup>a</sup>, B. Stover<sup>a</sup>, N. Afsar Kazerooni<sup>a</sup>, A. Srinivasa<sup>a</sup>, M. Hajhashemkhani<sup>b</sup>, M.R. Hematiyan<sup>b</sup>, S. Goenezen<sup>a,\*</sup>

<sup>a</sup> Department of Mechanical Engineering, Texas A & M University, College Station, 77843 Texas, USA

<sup>b</sup> Department of Mechanical Engineering, Shiraz University, Shiraz 71936, Iran

### ARTICLE INFO

#### Keywords:

Inverse problem in nonlinear elasticity  
Geometric nonlinearity  
Nonhomogeneous material characterization  
Silicone composite materials  
Digital image correlation

### ABSTRACT

A comparative study is presented to solve the inverse problem in elasticity for the shear modulus (stiffness) distribution utilizing two constitutive equations: (1) linear elasticity assuming small strain theory, and (2) finite elasticity with a hyperelastic neo-Hookean material model. Assuming that a material undergoes large deformations and material nonlinearity is assumed negligible, the inverse solution using (2) is anticipated to yield better results than (1). Given the fact that solving a linear elastic model is significantly faster than a nonlinear model and more robust numerically, we posed the following question: How accurately could we map the shear modulus distribution with a linear elastic model using small strain theory for a specimen undergoing large deformations? To this end, experimental displacement data of a silicone composite sample containing two stiff inclusions of different sizes under uniaxial displacement controlled extension were acquired using a digital image correlation system. The silicone based composite was modeled both as a linear elastic solid under infinitesimal strains and as a neo-Hookean hyperelastic solid that takes into account geometrically nonlinear finite deformations. We observed that the mapped shear modulus contrast, determined by solving an inverse problem, between inclusion and background was higher for the linear elastic model as compared to that of the hyperelastic one. A similar trend was observed for simulated experiments, where synthetically computed displacement data were produced and the inverse problem solved using both, the linear elastic model and the neo-Hookean material model. In addition, it was observed that the inverse problem solution was inclusion size-sensitive. Consequently, an 1-D model was introduced to broaden our understanding of this issue. This 1-D analysis revealed that by using a linear elastic approach, the overestimation of the shear modulus contrast between inclusion and background increases with the increase of external loads and target shear modulus contrast. Finally, this investigation provides valuable information on the validity of the assumption for utilizing linear elasticity in solving inverse problems for the spatial distribution of shear modulus associated with soft solids undergoing large deformations. Thus, this work could be of importance to characterize mechanical property variations of polymer based materials such as rubbers or in elasticity imaging of tissues for pathology.

© 2018 Elsevier Ltd. All rights reserved.

### 1. Introduction

Mapping the nonhomogeneous material property (here the shear modulus associated with the local material stiffness) distribution has potential applications in biomechanical engineering and clinical diagnosis, e.g. cancerous tumor detection [1–3], assessment of atherosclerosis [4,5], and the understanding of neurodegeneration. One approach to qualitatively infer the material property distribution non-destructively in the interior of a sample (away from the surface) uses axial strain maps and is often referred to as “elastography” [6,7]. This method assumes that the Young’s modulus can be interpreted to be inversely proportional

to the axial strain assuming that the stress is constant everywhere. The strain fields are computed using full-field displacement measurements acquired non-destructively by a variety of imaging modalities such as ultrasound [2,8–10], magnetic resonance imaging (MRI) [1], or computerized tomography (CT) scan [11]. Alternatively, the material property distribution can be recovered by modeling the mechanical behavior of the specimen or tissue and solving an inverse problem from known displacement fields and boundary conditions [12–16]. In this paper, we assumed quasi static deformations and posed the inverse problem as a constrained minimization problem subject to the constraint of the equilibrium equations and boundary conditions. In past works for quasi

\* Corresponding author.

E-mail address: [sgoenezen@tamu.edu](mailto:sgoenezen@tamu.edu) (S. Goenezen).

stical problems, this inverse mapping approach was used to determine linear elastic property distributions and nonlinear elastic property distributions for hyperelastic materials [13,16–19].

Generally, an empirical constitutive model that can describe the mechanical behavior of the solid is assumed to be known *a-priori*. Consequently, the choice of the constitutive model will affect the quality and accuracy of material property maps to characterize the mechanical behavior of the specimen. However, most inverse solvers are developed for linear elastic material modeling assuming small strain theory. This may raise the question on how well the inverse solution from the linear model represents the nonlinear mechanical behavior. This may depend on the overall deformations applied, i.e. at small strains the material will likely behave like a linear elastic solid and large deformation modeling may not be of interest for certain materials and applications. It will also depend on the degree of nonlinearity of the material, meaning that some materials may experience a nonlinear mechanical response starting at about 50% strain (many rubber like materials), while other materials may experience a nonlinear mechanical response starting at about 10% strain (for example breast tissues or blood vessels).

While modeling material nonlinearity is an important aspect when solving inverse problems, nonlinearity arising due to large deformations may introduce another source of uncertainty when using linear elasticity assuming small strain theory. Large deformations induce geometric nonlinearity and require the use of large strain measures such as the Green Lagrange strain measure and specification of a proper stress measure, for example, the first or second Piola Kirchhoff stress tensor. The equations of equilibrium are often written in the material coordinate system and the integral in the weak form is expressed over the undeformed configuration. This results in a nonlinear set of equations that can be discretized with Galerkin's method, linearized, and solved using the Newton–Raphson method. The geometric nonlinearity introduced via large deformations clearly adds significantly more complexity and computational cost to the solution of the inverse problem in elasticity.

In this paper, we investigate the validity of using a linear elastic model based on small strain theory to map the shear modulus distribution of a composite based silicone sample undergoing large deformations. The displacement field was measured using a digital image correlation system. The results from the linear elastic model were compared to the shear modulus maps obtained by solving the inverse problem with a neo-Hookean hyperelastic material model. In Section 2, the experimental set-up to measure full-field displacement data and the theoretical background of the linear and nonlinear elastic inverse methods will be discussed. In Section 3, the shear modulus reconstructions in 2-D for experimental and synthetic data are presented followed by a 1-D theoretical analysis. We discuss our results in Section 4 and conclude this work in Section 5.

## 2. Methods

### 2.1. Composite sample and digital imaging data acquisition

A composite membrane based on silicone materials, having a thickness of 0.6 cm and consisting of two cylindrical inclusions with 2.8 cm and 2.1 cm diameters were manufactured with dimensions shown in Fig. 1(a). The background material was made of ECOFLEX 00-10 and the inclusion material was made of ECOFLEX 00-50, varying the shear modulus between inclusion and background material. The same materials were also used to construct homogeneous samples to determine their material properties from their stress-stretch behavior from uniaxial tensile tests for later validation of our inverse solutions. The homogeneous specimens were prepared with dimensions of  $10 \times 2 \times 0.6$  cm for height  $\times$  width  $\times$  thickness. In order to prevent the sample from slipping between grips, small wooden pieces were glued to the sample ends. The uniaxial tensile tests were performed at room temperature with an INSTRON 5567 machine with wedge action grips. The gauge length was defined at 8 cm with 1 cm offset from the grips to avoid boundary effects

and bulging near the grips. The loading was displacement controlled at a deformation rate of 10 mm/min, sufficiently slow to avoid viscoelastic effects. The stress-strain response for inclusion and background materials are shown in Fig. 1(b). We note that the stress here represents the Cauchy stress for which the measured force is divided by the current area at the midsection of the specimen of the deformed or current configuration. From the slope of these curves, we determined the shear modulus of the inclusions to be approximately 2.5 times larger than their background material. We also observe that the stress-stretch curves of both materials are nearly linear, thus material nonlinearity is insignificant even for large strains of up to 30% for these materials.

In the following, we briefly describe the procedure to manufacture the composite samples. A custom wooden mold was used for making the composite sample and is shown in Fig. 2(a). ECOFLEX 00-10 was used for the background material and ECOFLEX 00-50 was used for the inclusions. Both materials are supplied as two parts and were mixed according to manufacture specification (equal parts). Afterwards, white Silc-Pig color was added to each mixture to color the sample white and provide a good contrast for the digital image correlation pattern applied to the surface (discussed below). The mixture was thoroughly mixed for about 3 minutes and then placed into a vacuum chamber to eliminate any entrapped air from the mixture. Then the liquid mixture with ECOFLEX 00-10 was poured into the mold shown in Fig. 2(b). The mixture was poured around two PVC cylindrical tubes to preserve space for the inclusions. After about three hours of curing at room temperature, the two cylindrical tubes shown in Fig. 2(b) were removed from the mold. The mixture for the inclusions, prepared after the tubes were removed, was then poured into the cylindrical voids. Curing at room temperature was allowed for about three hours followed by post curing of the sample in a heated chamber at 80 °C for two hours and 100 °C for one hour. The sample was then removed from the hot chamber to cool to room temperature and is shown in Fig. 2(c) post curing.

A digital image correlation (DIC) system (DANTEC DYNAMICS, Germany) consisting of two cameras, a light source, a calibration plate, and a laptop with the “Istra 4D” software was used in this work to measure full field displacement data of the composite silicone material in two-dimensional space. This system relies on random speckle patterns applied onto the sample's surface prior to data collection. Camera images were then recorded of the pre- and post-deformed sample and the displacement field calculated with the “Istra 4D” software by tracing and cross-correlating pre- and post-deformed speckle patterns. DIC technology is based on tracking unique features on the surface of the sample during deformation. Black spray paint was used to create the random dot pattern on the composite sample's face as shown in Fig. 3(a). The black speckle pattern on the sample's white color provides an optimum contrast for pattern feature tracking.

To deform the composite silicone sample, we utilized the same INSTRON machine introduced earlier for the homogeneous samples, shown in Fig. 3(b) with the composite sample during tensile testing. The bottom edge of the sample is fixed and a simple tensile force was applied to the top edge. In order to prevent the sample from slipping between grips, small wooden pieces were glued to the sample's ends (see Fig. 3(b) and (c)). The region of interest was about 1 cm offset from the top and bottom boundaries to avoid potential bulging in the data. The camera system was placed in near proximity to the INSTRON machine, shown in Fig. 3(c). The aperture and focus on each camera was adjusted and the light source was aimed on the sample's surface to ultimately obtain images with maximum contrast. Afterwards, the DIC camera system was calibrated to identify internal system parameters and the relative position of the two cameras to each other. The calibration plates provided with the DIC system come in different sizes, and a suitable calibration plate size is one that covers the entire field of view of the cameras. Fig. 3(d) represents an image taken during the calibration process. After successfully completing the calibration process, a set of images were recorded followed by sequence of images recorded while the sample was deformed with the INSTRON machine. The deformation was displace-

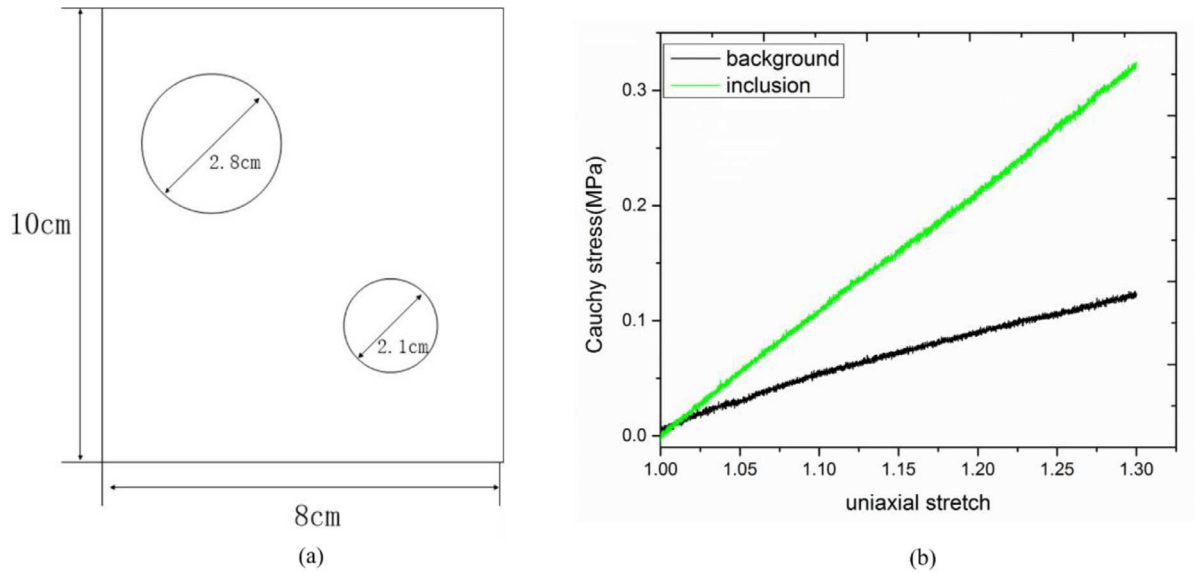


Fig. 1. (a) The dimensions of the composite material; (b) plots of Cauchy stress versus the stretch of background material and inclusion material.

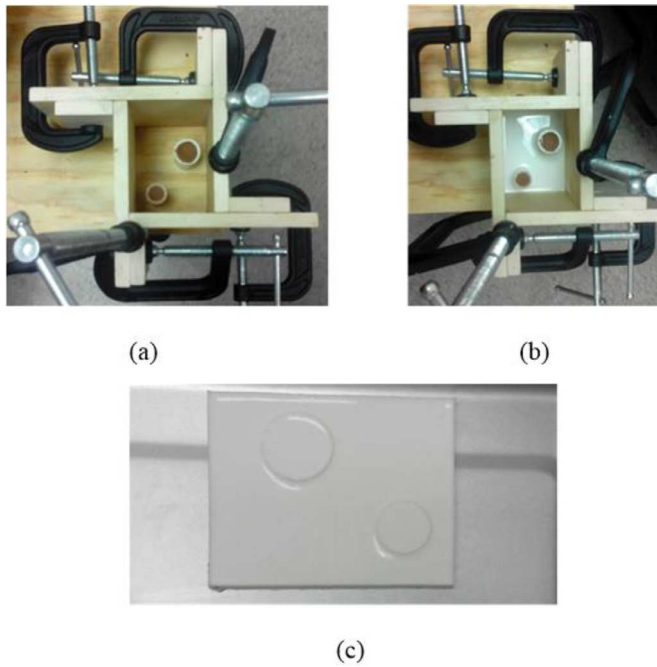


Fig. 2. Manufacturing of the composite sample. (a) The mold for composite sample. (b) The background solution poured into the mold. (c) The final post-cured composite sample.

ment controlled at a rate of 10 mm/min and experiments were done under room temperature, thus viscoelastic effects could be assumed negligible. The Istra 4D software was then used to analyze the images and calculate displacements on grid points with predefined spacing. The Istra 4D software divides the images into sub-images called facets that contain a collection of dots to calculate displacements based on sub-image similarities between pre- and post-deformed images. Fig. 3(e) depicts the displacement plot of the sample after post-processing with the Istra 4D software.

### 2.2. Modulus reconstruction

After acquiring the full field displacement field in the entire region of interest of the sample, the shear modulus distribution can be recovered utilizing an in-house written regularized inverse method discussed in [12] and tested for an exponential strain energy density function with simulated data therein. Briefly, the inverse problem is posed as a constrained optimization problem where the following objective function is minimized:

$$F = \frac{1}{2} \|(\mathbf{u}(\mu(\mathbf{x}), \mathbf{x}) - \mathbf{u}_{meas}(\mathbf{x}))\|_0^2 + \frac{1}{2} \alpha \text{Reg}(\mu(\mathbf{x})) \quad (1)$$

subject to the constraint that the measured displacement vector  $\mathbf{u}_{meas}$  and the computed displacement vector  $\mathbf{u}$  are minimized in the L2 norm. The second term is the regularization term which is a function of the shear modulus  $\mu(\mathbf{x})$ , and the regularization factor  $\alpha$  controls the weight of the regularization term. The spatial coordinate is denoted by  $\mathbf{x}$ . In this paper, the total variation diminishing (TVD) regularization has been adopted, and its specific expression can be found in [12,15,20]. Eq. (1) is discretized with finite element based bilinear shape functions and the shear modulus distribution is assumed to be continuous in the problem domain with unknown shear modulus values defined on the mesh nodes. Thus the total number of optimization parameters is equal to the total number of mesh nodes. The constrained optimization problem is solved by the limited-BFGS method [21,22] for which we evaluate the gradient of the function with respect to the nodal shear modulus unknowns. To efficiently evaluate this gradient vector, we employ the adjoint method [12,17]. As the mathematical foundation and numerical procedures of the inverse algorithms have been thoroughly discussed in [12], it will not be elaborated herein.

We adopted a simple isotropic and linear elastic material model assuming small strain theory and a hyperelastic model to study the mechanical behavior of the silicon sample undergoing large deformations. As the stress-strain relations of both the background and the inclusion materials are nearly linear even for larger deformations of about 30% strain as shown in Fig. 1(b), we utilized the simplest hyperelastic model, the neo-Hookean model, to study the nonlinear elastic behavior of the phantom. The strain energy density function for an incompressible neo-Hookean solid is given by:

$$W = \frac{\mu}{2} (J^{-2/3} I_1 - 3) \quad (2)$$

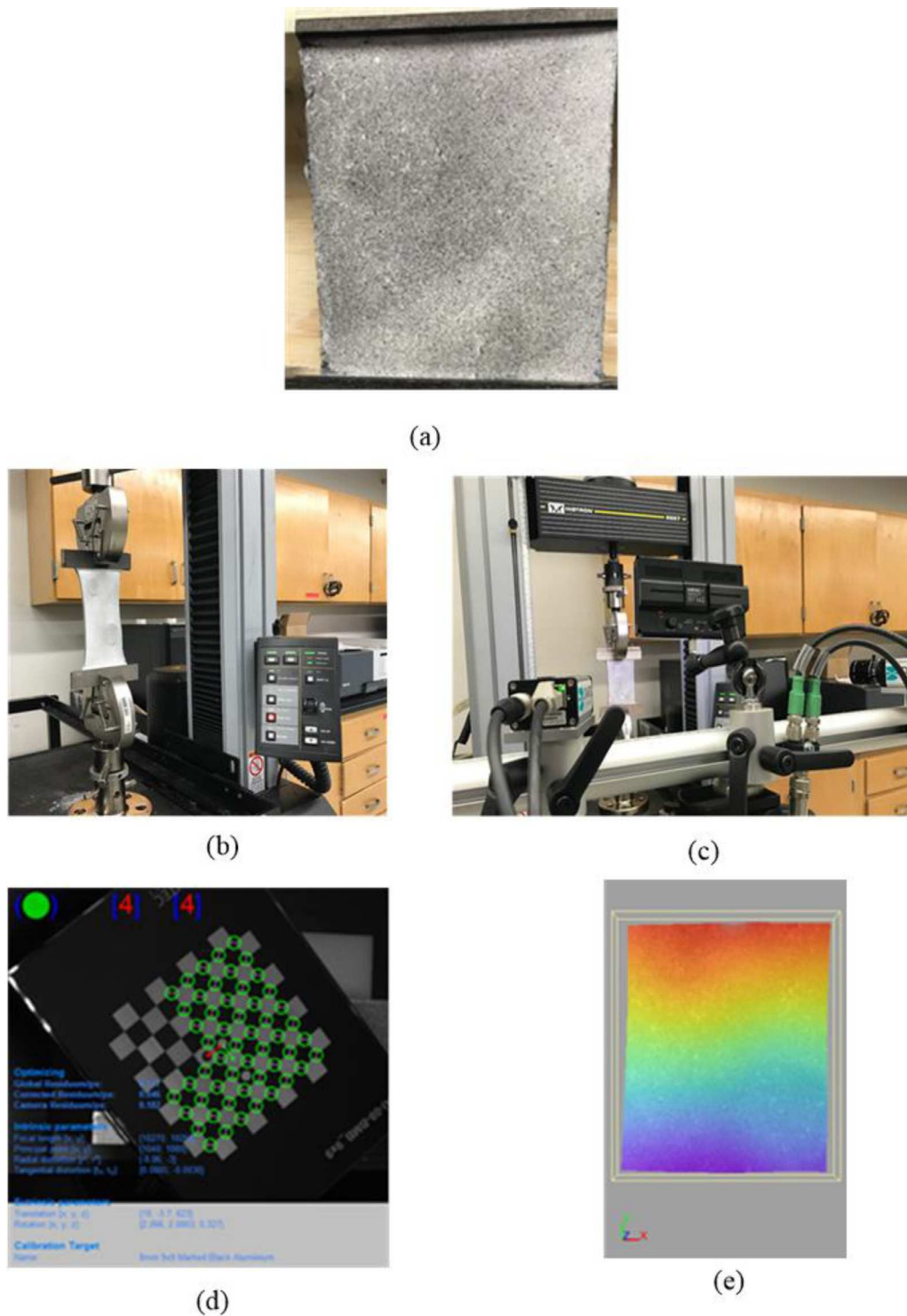


Fig. 3. (a) Random dot pattern on face of composite sample. (b) Composite sample during deformation with INSTRON machine. (c) DIC system used to record images during sample deformation. (d) Calibration of the system using calibration plates in process. (e) Displacement plot of the sample analyzed with Istra 4D software.

where,  $J$  and  $I_1$  are the determinant of the deformation gradient and the first invariant of the right Cauchy-Green deformation tensor, respectively. It is straightforward to derive the associated Cauchy stress and 2nd Piola–Kirchhoff stress tensors.

To compare the difference in mechanical behavior between a linear elastic and neo-Hookean material model, we plot the stress versus stretch curve in Fig. 4 for uniaxial tension assuming a shear modulus value of  $\mu=1$ . We observe that these two curves nearly coincide for

strains up to about 20% and the curve from the neo-Hookean model slightly deviates from the linear curve between the strain range of 20–50%. We note that for finite deformations, the integral in the weak form distinguishes between a deformed and undeformed problem domain, while for small strain theory this distinction is not being made. That introduces additional geometric nonlinearities and may affect the solution to the inverse problem in elasticity. In this work, we investigated

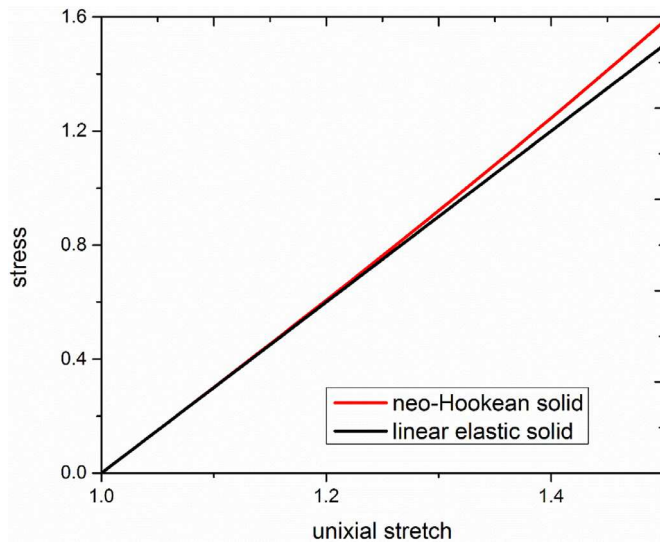


Fig. 4. Plots of uniaxial stress versus stretch curves for a neo-Hookean and a linear elastic solid. The shear modulus is set to 1.

the uncertainties introduced when assuming small strain theory for a problem that actually undergoes large deformations.

### 3. Results

In the following simulations, we assumed that the material was incompressible in three-dimensional space, which is a good assumption for silicone based materials. Further, we modeled the membrane in two-dimensional space assuming plane stress theory. This is a reasonable assumption, since the membrane is relatively thin and no tractions are acting on its front and back faces. For all computations presented in this section, the constrained minimization problem was considered to be converged when the objective function (see Eq. (1)) value did not drop significantly beyond machine precision. Also, the measurement points on the sample, i.e., grid points at which displacement values were correlated, coincided with the finite element nodes of the simulations for the experimental and synthetic data.

#### 3.1. Modulus reconstruction of a silicone based composite sample with DIC displacement data

We first solved the inverse problem for the silicone based composite sample and compared the differences in the shear modulus reconstructions using the linear elastic and neo-Hookean model. For the inverse problem, the problem domain of interest (see Fig. 3(a)) was discretized with 1221 bilinear elements, and only the vertical displacement component was used as measured data to show feasibility of this method with limited data only. For the boundary conditions, displacements in both directions on all four edges of the problem domain were prescribed. As only displacement data were utilized to solve the inverse problem and no traction information was prescribed, the shear modulus distribution was mapped only up to a multiplicative factor. Fig. 5 shows the shear modulus reconstructions utilizing the linear elastic and the neo-Hookean model for displacement data collected at about 2% overall strain. In this case, the regularization factor for both cases were selected to be  $6.0 \times 10^{-4}$ . The objective function value dropped relative to its initial value by 81.02% and 65.21% after a total number of 205 and 185 iterations for the linear elastic and neo-Hookean model, respectively. It is apparent that both the linear elastic and the neo-Hookean models are capable of detecting the location and preserving the shape of these two inclusions well. However, employing the linear elastic model lead to higher shear modulus values in the inclusions as compared to the inclu-

sion shear modulus values obtained using the neo-Hookean model. Both methods have in common that the recovered shear modulus value in the smaller inclusions was significantly underestimated.

Fig. 6 represents shear modulus reconstructions utilizing the linear elastic and neo-Hookean models for the case when the composite silicone sample undergoes large deformations of about 18%. The regularization factor utilized for both cases were chosen to be  $7.0 \times 10^{-3}$ . The objective function value dropped relative to its initial value by 88.21% and 77.31% after a total number of 244 and 200 iterations for the linear elastic and neo-Hookean model, respectively. We observed a similar trend to Fig. 5 in that the shear modulus values in the inclusions using the linear elastic model were higher than the shear moduli predicted by the neo-Hookean model.

#### 3.2. Modulus reconstruction obtained with simulated experiments

We also created simulated data to solve the inverse problem to evaluate this procedure with exactly known ground truth. The simulated data was obtained by solving the forward problem using finite element methods and assuming a neo-Hookean material model. To this end, a unit square problem domain (see Fig. 7(a)) with two inclusions having different sizes and resembling the problem geometry of the silicone composite sample used in the previous section has been defined and discretized with 3600 bilinear elements. The shear moduli for the inclusions were prescribed to be 2 times stiffer than the background material. The boundary conditions for the forward problem were prescribed with uniform extension on the top edge and the bottom edge was restricted and fixed in its vertical motion. To avoid rigid body motion, the center node of the bottom edge was fixed in both displacement components. In solving the inverse problem, we utilized the same displacement boundary conditions prescribed in the forward problem. Additionally, we added 3% random noise to the displacement data to simulate noisy measurements, and assumed that the vertical full field displacement component is only known.

Fig. 7 depicts the reconstructed shear modulus distributions for a simulated overall strain of about 2%, using the linear elastic and neo-Hookean model with a regularization factor of  $10^{-8}$ . The objective function value dropped relative to its initial value by 62.96% and 56.69% after a total number of 2362 and 2825 iterations for the linear elastic and neo-Hookean model, respectively. It was observed that the shape and location of both, small and large inclusions were well recovered. We also observed that the values of the shear moduli in the inclusions are higher for the linear elastic model compared to those predicted using the neo-Hookean model. In addition, the recovered shear modulus in the smaller inclusion is smaller than that in the large inclusion. These trends were also observed for the results obtained with the experimental data in the previous section. For a large deformation of about 15% overall strain, the reconstructed shear modulus distributions are shown in Fig. 8 for a regularization factor of  $5.0 \times 10^{-7}$  for both models. The objective function value dropped relative to its initial value by 64.96% and 58.89% after a total number of 2382 and 2618 iterations for the linear elastic and neo-Hookean model, respectively. It was observed that the shear moduli in the inclusions for the linear elastic model are also higher than those using the neo-Hookean model. Overall, the reconstructions utilizing simulated data exhibit a very similar trend to what we observed with the experimental data.

#### 3.3. Modulus reconstruction via a 1-D coupled model

To represent a large number of cases with varying target shear moduli, we utilized a 1-D coupled model for analysis shown in Fig. 9. To investigate the issue of smaller stiffness contrast in the smaller inclusion, we assumed that the two bars follow the linear elastic model instead of the neo-Hookean model, since the linear elastic problem is easier to solve and this issue occurred for both constitutive equations. As this 1-D coupled model represented the 2-D model well in past studies and has

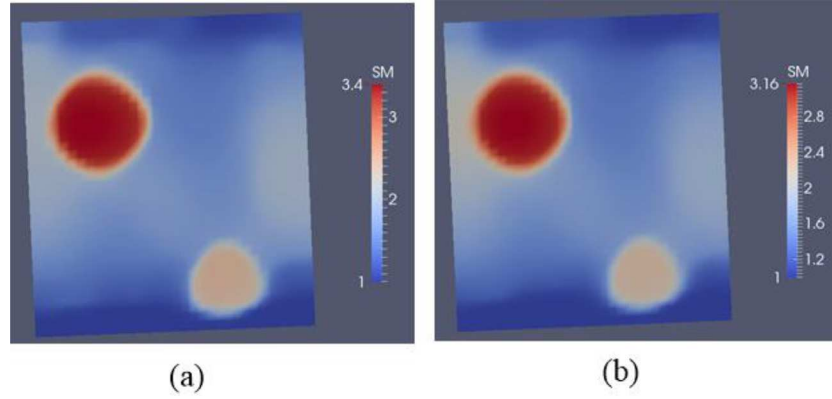


Fig. 5. Shear modulus reconstructions of the silicone based composite sample utilizing an overall strain of 2% and a regularization factor of  $6.0 \times 10^{-4}$  with (a) a linear elastic model, (b) a neo-Hookean model.

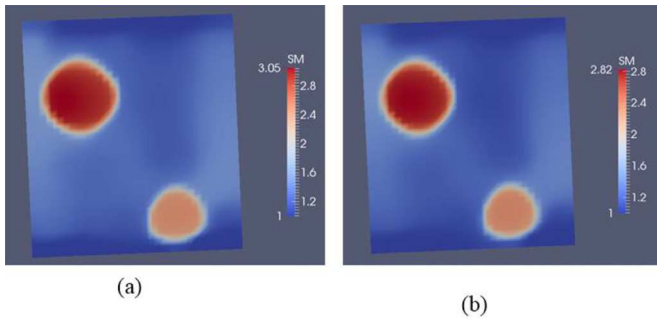


Fig. 6. Shear modulus reconstructions of the silicone based composite sample utilizing an overall strain of 18% and a regularization factor of  $7.0 \times 10^{-3}$  with (a) a linear elastic model, (b) a neo-Hookean model.

been thoroughly discussed in [15], we will skip the discussion here and directly employ the relation between the left and right bars presented in Fig. 9, derived in [15]:

$$\frac{t^1}{3(\mu_{in}^1(-1+a^1)-a^1)^3(\bar{\mu}_{in}^1(-1+a^1)-a^1)} = \frac{t^2}{3(\mu_{in}^2(-1+a^2)-a^2)^3(\bar{\mu}_{in}^2(-1+a^2)-a^2)} \quad (3)$$

where

$$t^i = +u^i a^i \mu_{in}^i (-\bar{\mu}_{in}^i (u^i - n \cdot \bar{u}^i) (-1 + a^i) \left( (-1 + a^i)^3 + 3b^i (-1 + a^i) a^i + 3(b^i)^2 (1 + a^i) \right) + u^i (a^i)^2 \mu_{in}^i (-n \cdot u_{exact}^i (-1 + a^i))$$

$$\begin{aligned} & \left( 3 + 3(b^i)^2 + 3b^i(-2 + a^i) - 4a^i + (a^i)^2 \right) \\ & + (u^i)^2 (a^i)^2 \mu_{in}^i \left( (-1 + a^i)^3 + 3b^i(-1 + a^i) a^i + 3(b^i)^2 (1 + a^i) \right) \\ & + u^i (a^i)^2 \mu_{in}^i (-u^i - n \cdot \bar{u}^i) a^i \left( 3 + 3(b^i)^2 + 3b^i(-2 + a^i) - 4a^i + (a^i)^2 \right) \\ & + (u^i)^2 (a^i)^2 \mu_{in}^i \bar{\mu}_{in}^i \left( (-1 + a^i) \left( 3(-1 + a^i)^2 + (-4 + 3a^i) a^i + (a^i)^2 \right) \right) \\ & + u^i (a^i)^2 \mu_{in}^i \bar{\mu}_{in}^i (-n \cdot \bar{u}^i \left( (-1 + a^i)^3 + 3b^i(-1 + a^i) a^i + 3(b^i)^2 (1 + a^i) \right)) \end{aligned} \quad (4)$$

and  $i=1, 2$ .  $n$  is the noise factor which was set to 1 herein assuming that no noise is introduced in the measured displacements.  $\bar{\mu}_{in}^i$  is the exact shear modulus of the inclusion, and  $\bar{\mu}_{in}^1 = \bar{\mu}_{in}^2$  is consistent with the 2-D numerical examples presented earlier. The background of the bar has a shear modulus value of 1.  $\mu_{in}^i$  is the recovered shear modulus for each inclusion. The length  $a^i$  ( $i=1, 2$ ) is analogue to the stiff inclusion diameter, and we assume  $a^1 > a^2$  to be consistent with the 2-D model. In addition, the prescribed displacements  $\bar{u}^1 = \bar{u}^2 > 0$ . Next, we assumed that the recovered shear modulus of the larger inclusion is 20% off, that is,  $\mu_{in}^1 = 0.8\bar{\mu}_{in}^1$ . Thereby, the mapped shear modulus of the smaller inclusion could be evaluated by Eq. (4). One may expect the shear modulus of the right inclusion to be consistently off by 20% as well. Thus, deviations from this expected value were defined as the relative error given by  $[(\mu_{in}^2 - 0.8\bar{\mu}_{in}^2)/(0.8\bar{\mu}_{in}^2)]100\%$ , i.e., a negative relative error revealed that the shear modulus of the small inclusion was underestimated more than the shear modulus of the large inclusion. Fig. 10 plots this relative error over the target shear modulus values in the inclusions for two scenarios. The red line represents the case where the two inclusions are located in the center of the two bars, respectively. The prescribed parameters used in this case are:  $a^1 = 0.4$ ,  $a^2 = 0.2$ ,  $b^1 = 0.3$ ,  $b^2 = 0.4$ . The green line corresponds to the case where small and large inclusions are placed downwards and upwards, respec-

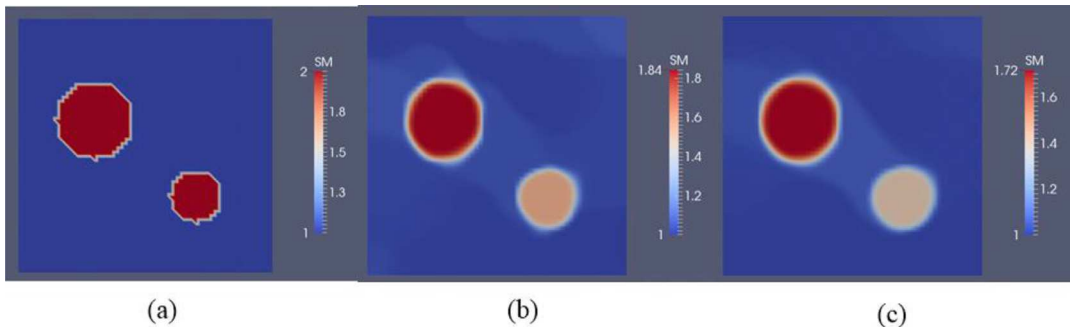


Fig. 7. (a) Target shear modulus distribution. Shear modulus reconstructions based on simulated experiments utilizing an overall strain of 2% and a regularization factor of  $10^{-8}$  with (b) a linear elastic model; (c) a neo-Hookean model.

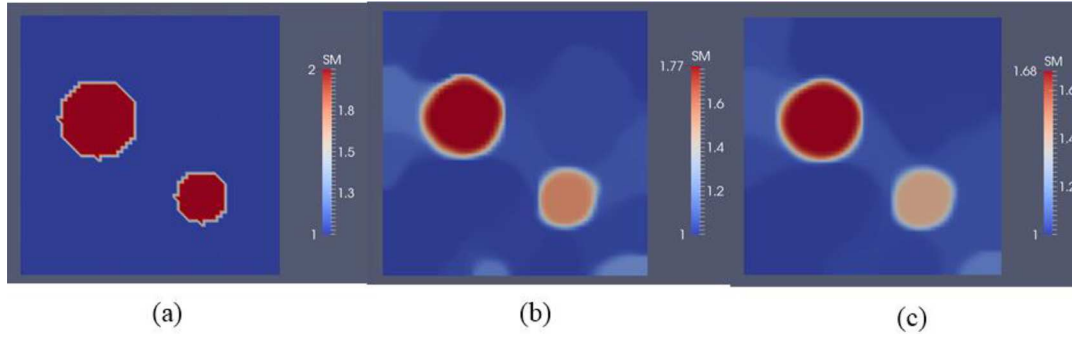


Fig. 8. (a) Target shear modulus distribution. Shear modulus reconstructions based on simulated experiments utilizing an overall strain of 15% and a regularization factor of  $5.0 \times 10^{-7}$  with (b) a linear elastic model; (c) a neo-Hookean model.

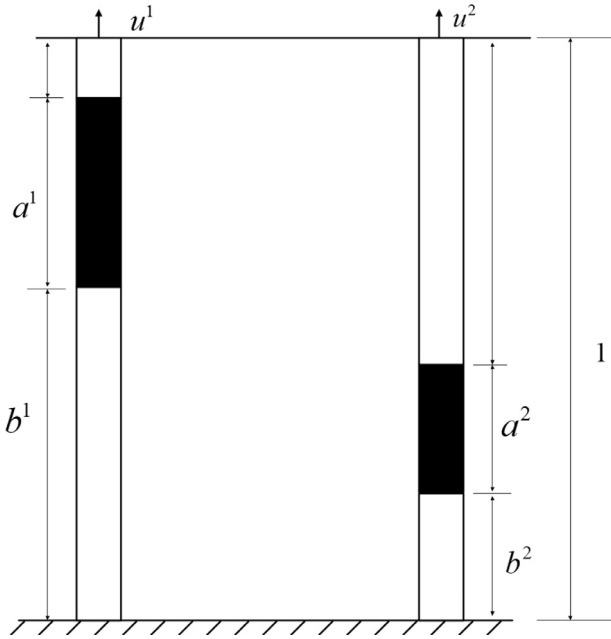


Fig. 9. A coupled 1-D model: two linearly elastic and nonhomogeneous bars connected by two rigid plate.

tively, that is,  $a^1 = 0.4$ ,  $a^2 = 0.2$ ,  $b^1 = 0.5$ ,  $b^2 = 0.3$ . We observed that the relative error was always negative, which means that the smaller inclusion was underestimated more than the large inclusion. Furthermore, this underestimation became more significant when the two inclusions were placed diagonally.

### 3.4. Effects of linear elastic assumption for geometric nonlinear constitutive model analysis via a 1-D model

To analyze the effect of using a linear elastic model to solve the inverse problem for a solid undergoing geometric nonlinearity, we considered a 1-D problem that would allow us to represent a large number of cases with varying target shear moduli. To this end, we defined a bar shown in Fig. 11, where the stiffness of the black and white regions are denoted by  $\bar{\mu}_{in}$  and  $\bar{\mu}_b$ , respectively. The black and white regions mimic the inclusion and background in two-dimensional cases, respectively. We fix the bar at its bottom end and apply a displacement of  $u_e$  at the top end. The total length of the bar is denoted by  $L$ , the length of the black region is represented by  $a$ , and the distance between the bottom end of the black region and the fixed end of the bar is denoted by  $b$ . Given that the stretches are piecewise constants in the black and white

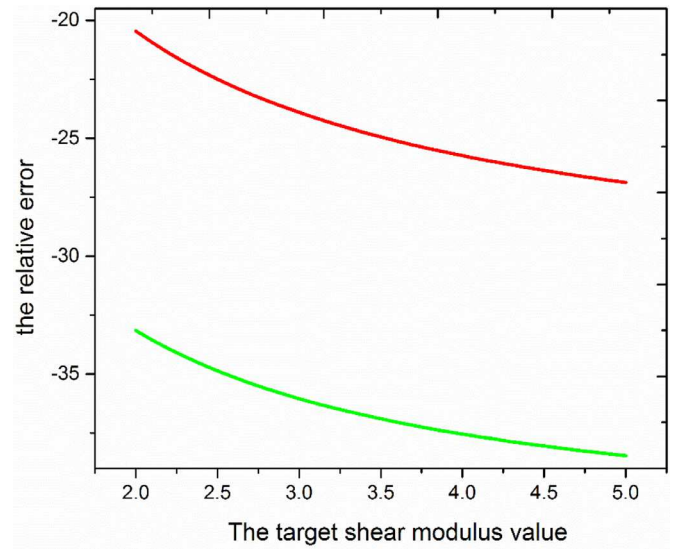


Fig. 10. The relative error over different target shear modulus values in inclusions. Red line represents the case where the two inclusions are located in the center of the two bars. Green line corresponds to the case where small and large inclusions are placed downwards and upwards, respectively. (For interpretation of the references to color in this figure legend, the reader is referred to the web version of this article.)

regions, one can yield the displacement field  $u_{exact}$  along the bar:

$$u_{exact} = \begin{cases} b \cdot \lambda_b + a \cdot \lambda_{in} + (y - b - a)\lambda_b - y & \text{when } b + a < y \leq L \\ b \cdot \lambda_b + (y - b)\lambda_a - y & \text{when } b < y \leq b + a \\ y \cdot \lambda_b - y & \text{when } 0 < y \leq b \end{cases} \quad (5)$$

where  $\lambda_a$  and  $\lambda_b$  are stretches in the inclusion and background, respectively. Since the 2nd Piola–Kirchhoff stress of the inclusion equals that of the background due to the constant axial force in the bar, one can derive the following relationship between  $\lambda_a$  and  $\lambda_b$ :

$$\bar{\mu}_{in} \left( 1 - \frac{1}{\lambda_a^3} \right) = \bar{\mu}_b \left( 1 - \frac{1}{\lambda_b^3} \right) \quad (6)$$

Moreover, the displacement on the top end of the bar is  $u_e$ , thus leading to another relation between  $\lambda_a$  and  $\lambda_b$ , that is:

$$u_e = \lambda_a a + \lambda_b (L - a) - L \quad (7)$$

Thereby, with the assistance of Eqs. (6) and (7), we are capable of acquiring  $\lambda_a$  and  $\lambda_b$ , and further determining the displacement field  $u_{exact}$  by virtue of Eq. (5). The displacement field  $u_{exact}$  is used as the measured displacement in the inverse problem. The objective function in the 1-D

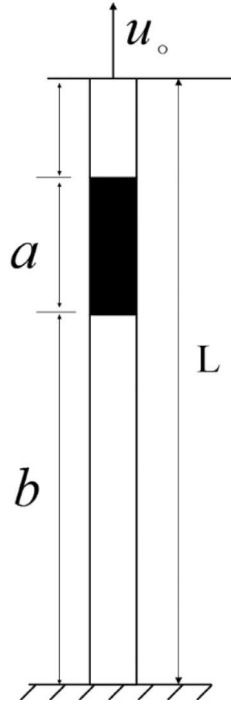


Fig. 11. 1-D nonhomogeneous elastic bar subject to uniaxial extension.

case can be written as

$$F = \frac{1}{2} \int_0^1 (u_{com} - u_{exact})^2 dy + \alpha |\mu_{in} - \mu_b| \quad (8)$$

where  $\mu_b$  and  $\mu_{in}$  are the estimated stiffness of the background and inclusion, respectively. In addition,  $u_{com}$  represents the computed displacement. The formula of the 1-D objective function has been thoroughly discussed in [15]. Clearly,  $\mu_{in} = \bar{\mu}_{in}$  and  $\mu_b = \bar{\mu}_b$  when  $\alpha = 0$  and the same constitutive model is used to predict the mechanical response of the bar in the inverse problem. However, adopting the linearized strain measure to solve the inverse problem yields the following computed displacement field  $u_{com}$ :

$$u_{com} = \begin{cases} b \cdot \epsilon_b + a \cdot \epsilon_{in} + (y - b - a)\epsilon_b^i & \text{when } b + a < y \leq 1 \\ b \cdot \epsilon_b + (y - b)\epsilon_{in} & \text{when } b < y \leq b + a \\ y \cdot \epsilon_b & \text{when } 0 < y \leq b \end{cases} \quad (9)$$

where  $\epsilon_b$  and  $\epsilon_{in}$  are the computed strains of the background and inclusion, respectively. As the stress in this bar is constant, we have the relationship  $\mu_{in}\epsilon_{in} = \mu_b\epsilon_b$ . Combining this relationship with the kinematic constraint yields the explicit expression of  $\epsilon_b$  and  $\epsilon_{in}$ :

$$\begin{aligned} \epsilon_b &= u_o / ((L - a) + a\mu_b/\mu_{in}) \text{ and} \\ \epsilon_{in} &= u_o / ((L - a)\mu_{in}/\mu_b + a) \end{aligned} \quad (10)$$

We also fix  $\mu_b = 1$  as the stiffness distribution is relatively mapped. Thereby, the objective function is merely a function of the inclusion stiffness  $\mu_{in}$ . Minimizing the objective function yields the following equation:

$$\frac{\partial F}{\partial \mu_{in}} = 0 \quad (11)$$

which can be utilized to determine the inclusion stiffness  $\mu_{in}$ . Fig. 12 exhibits the recovered inclusion stiffness over various external displacements from 0.02 L (2% deformation) to 0.2 L (20% deformation) for different exact inclusion stiffness  $\bar{\mu}_{in}$  ( $= 2, 3, 4, 5$ ) when the regularization factor  $\alpha$  is set to zero. In this case, other parameters utilized in Fig. 12 are as follows:  $L = 1$ ,  $a = 0.2$ , and  $b = 0.4$ .

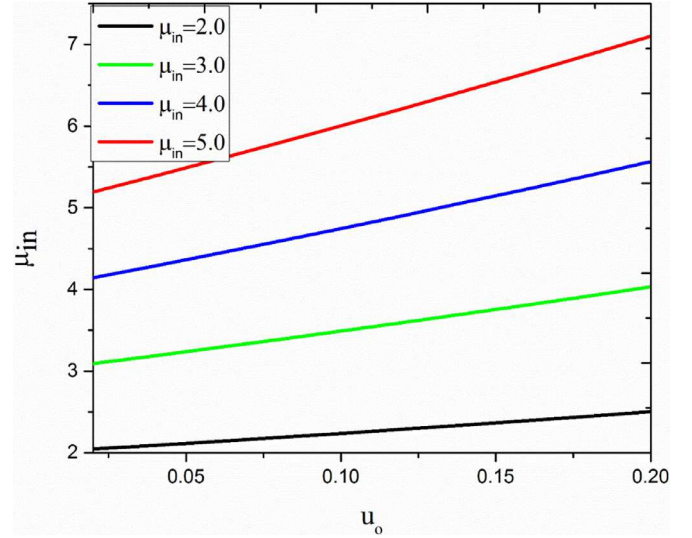


Fig. 12. Plot of the reconstructed shear modulus in the inclusion over the external displacements at the top end of the bar for different exact stiffness values in the inclusion  $\bar{\mu}_{in}$  ( $= 2, 3, 4, 5$ ).

#### 4. Discussion

In this work, we utilized an iterative approach to solve inverse problems in elasticity using a linear and a hyperelastic (neo-Hookean) model with experimental and simulated data. The measured data sets were acquired using a digital image correlation system and the simulated data sets were acquired by solving the forward problem for a neo-Hookean material model using finite element methods. We compared the reconstructed shear modulus distributions using a linear elastic and a neo-Hookean model on a composite problem domain undergoing small and large deformations. This work provides insight into the effects of using a linear elastic material model to solve the inverse problem for the shear modulus for materials undergoing large deformations. Assuming that the material behaves like a neo-Hookean solid, it appears that the inverse solution based on a linear elastic model provides reasonable results for large deformations of about 18% and 15% overall strain utilized in our experimental and simulated examples in Sections 3.1 and 3.2, respectively. We note that solving the inverse problem with the linear elastic model is computationally faster by about one order and the finite element solution is more robust as well.

In Section 3.1, we solved the inverse problem by utilizing experimental data on a composite silicone sample with two stiff inclusions embedded in a softer background. The shear modulus contrasts between inclusions and background was about 2.5. The displacement field of the sample was measured using a digital imaging correlation (DIC) system. The accuracy of the DIC system to measure surface displacements was analyzed in [23]. In solving the inverse problem, we specified the entire displacement boundary of the problem domain and assumed that the vertical displacement component was only known as measured data in the objective function. We observed that the inclusions were well recovered in both, shape and shear modulus values, despite the fact that the shear modulus contrasts between the inclusions and the background was quite low. We also observed that the shear modulus value in the smaller inclusion was significantly underestimated. Furthermore, comparing the reconstructions from both models, we observed that the shear modulus contrast for the linear elastic model was slightly larger than for the neo-Hookean model for the small and large deformation cases.

In Section 3.2, we presented a study performed on a simulated experiment that mimics the mechanical response of the composite silicone sample. In this case, measured displacement fields were obtained by solving a forward problem for a neo-Hookean solid subjected to small

and large deformations. We then added 3% noise to simulated displacements and solved the inverse problem for the shear modulus distribution using both linear and neo-Hookean models and utilizing only the vertical displacement component. We observed a similar trend to the results obtained with the experimental data in that (1) the shear modulus in the smaller inclusion was significantly more underestimated than the shear modulus in the larger inclusion, and (2) the linear elastic model had a slightly higher shear modulus values in the inclusions compared to the neo-Hookean model. To further investigate these observations and generate a broader spectrum of results for various target shear moduli, we developed a 1-D model in Section 3.3 to analyze case (1) and Section 3.4 to analyze case (2). Concerning (1), the 1-D model predicted a similar outcome as the 2-D model in that the smaller inclusion was significantly underestimated. Furthermore, Fig. 10 revealed that this underestimation grew with an increase in the shear modulus in the inclusion. We also observed that the location of the inclusions (horizontally aligned versus not aligned) makes a significant difference in how much the shear modulus of the smaller inclusion is underestimated relative to the larger inclusion.

Concerning (2), we utilized another 1-D model and observed that the reconstructed shear modulus obtained with the linear elastic model was slightly higher than the ground truth at 2% overall strain (see Fig. 12). This difference grows slowly and linearly with increasing deformations shown for up to 20% overall strain in the plot. Further, in Fig. 12 we also presented the cases with shear modulus values in the inclusion of 2, 3, 4, and 5 and observed that an increased shear modulus contrast leads to a higher increase of the reconstructed shear modulus using the linear elastic model (see slopes of the linear curves). Overall, our 1-D model represented trends observed in the 2-D simulations, in particular that the shear modulus reconstruction with the linear elastic model was slightly higher than the reconstruction from the neo-Hookean model. However, while the 1-D model suggests that this difference becomes increasingly larger, our 2-D simulations only revealed a slight difference. This could be a result of noise in measured data that was not taken into account in the 1-D model.

## 5. Conclusions

In this paper, we presented a comparative study to solve the inverse problem in elasticity using a linear elastic model and a neo-Hookean model for the shear modulus distribution using both, experimental and simulated measurements. We assumed that the material undergoes small (about 2% overall strain) and large (about 15% and 18% overall strain) deformations. The experimental data of a soft and nonhomogeneous phantom was obtained with high accuracy utilizing a digital image correlation system. The simulated measurements were created by solving a finite element problem. The shear modulus reconstructions for the simulated and experimental examples were well recovered with respect to size and location of the stiff inclusions for both, the linear elastic model and the non-linear elastic model. However, the linear elastic model overestimated the shear modulus values in the inclusions slightly relative to the reconstructions using the nonlinear model. To better analyze this, we performed a 1-D theoretical analysis to generalize the observation of the 2-D reconstruction to a broad number of shear modulus values. In this 1-D theoretical analysis, we also observed that the shear modulus contrast was overestimated when the linear elastic model was adopted. Overall, this work concludes that the linear elastic model may be utilized in the framework of this inverse problem solution procedure to solve the shear modulus distribution of a neo Hookean solid undergoing small and large deformations of up to 18%.

## Acknowledgment

We would like to acknowledge partial funding of this work from the Haythornthwaite Research Initiation Grant Award and from the National Science Foundation under Grant No. CMMI #1663435 and thank for their support.

## Reference

- [1] Venkatesh SK, Yin M, Glockner JF, Takahashi N, Araoz PA, Talwalkar JA, Ehman RL. Magnetic resonance elastography of liver tumors- preliminary results. *AJR. Am J Roentgenol* 2008;190(6).
- [2] Burnside ES, Hall TJ, Sommer AM, Hesley GK, Sisney GA, Svensson WE, Hangian-dreou NJ. Ultrasound strain imaging to improve the decision to biopsy solid breast masses. *Radiology* 2007;245(2):401–10.
- [3] Abbas Samani JZ, Plewes D. Elastic moduli of normal and pathological human breast tissues: an inversion-technique-based investigation of 169 samples. *Phys Med Biol* 2007;52:1565–76.
- [4] Richards MS, Doyley MM. Investigating the impact of spatial priors on the performance of model-based IVUS elastography. *Phys. Med. Biol.* 2011;56(22):7223–46.
- [5] Richards MS, Perucchio R, Doyley MM. Visualizing the stress distribution within vascular tissues using intravascular ultrasound elastography: a preliminary investigation. *Ultrasound Med Biol* 2015;41(6):1616–31.
- [6] Ophir J, Alam SK, Garra B, Kallel F, Konofagou E, Krouskop T, Varghese T. Elastography: ultrasonic estimation and imaging of the elastic properties of tissues. *Proc Inst Mech Eng H* 1999;213(3):203–33.
- [7] Ophir J, Cespedes I, Ponnekanti H, Yazdi Y, Li X. Elastography: a quantitative method for imaging the elasticity of biological tissues. *Ultrason Imaging* 1991;13(2):111–34.
- [8] Shapo BM, Crowe JR, Skovoroda AR, Eberle MJ, Cohn NA, O'Donnell M. Displacement and strain imaging of coronary arteries with intraluminal ultrasound. *IEEE Trans Ultrasonics Ferroelectr Freq Control* 1996;43(2):234–46.
- [9] Wilson LS, Robinson DE. Ultrasonic measurement of small displacements and deformations of tissue. *Ultrasonic Imaging* 1982;4(1):71–82.
- [10] Zaleska-Dorobisz A, Kaczorowski B, Pawluś A, Puchalska B, Ingłot B M. Ultrasound elastography – review of techniques and its clinical applications. *Brain* 2013;6:10–14.
- [11] Butcher JT, Sedmera D, Guldberg RE, Markwald RR. Quantitative volumetric analysis of cardiac morphogenesis assessed through micro-computed tomography. *Dev Dyn* 2007;236(3):802–9.
- [12] Goenezen S, Barbone P, Oberai AA. Solution of the nonlinear elasticity imaging inverse problem: the incompressible case. *Comput Methods Appl Mech Eng* 2011;200(13–16):1406–20.
- [13] Goenezen S, Dord JF, Sink Z, Barbone P, Jiang J, Hall TJ, Oberai AA. Linear and nonlinear elastic modulus imaging: an application to breast cancer diagnosis. *IEEE Trans Med Imaging* 2012;31(8):1628–37.
- [14] Goenezen S, Oberai AA, Dord J, Sink Z, Barbone P. Nonlinear elasticity imaging. In: *Proceedings of the IEEE thirty-seventh annual northeast bioengineering conference (NEBEC)*; 2011. p. 1–2.
- [15] Mei Y, Goenezen S. Spatially weighted objective function to solve the inverse problem in elasticity for the elastic property distribution. *Computational biomechanics for medicine: new approaches and new applications*. Doyle BJ, et al., editors. NY: Springer; 2015.
- [16] Oberai AA, Gokhale NH, Goenezen S, Barbone P, Hall T, Sommer AM, Jiang J. Linear and nonlinear elasticity imaging of tissue in-vivo: demonstration of feasibility. *Phys Med. Biol* 2009;54:1191–207.
- [17] Oberai AA, Gokhale NH, Feijóo GR. Solution of inverse problems in elasticity imaging using the adjoint method. *Inverse Probl* 2003;19(2):297.
- [18] Li D, Oberai A. Recovery of cellular traction in three-dimensional nonlinear hyper-elastic matrices. *Comput Methods Appl Mech Eng* 2016;314:296–313.
- [19] Tyagi M, Goenezen S, Barbone P, Oberai AA. Algorithms for quantitative quasi-static elasticity imaging using force data. *Int J Numer Methods Biomed Eng* 2014;30(12):1421–36.
- [20] Mei Y, Kuznetsov S, Goenezen S. Reduced boundary sensitivity and improved contrast of the regularized inverse problem solution in elasticity. *J Appl Mech* 2016;83(3):031001.
- [21] Zhu C, Byrd RH, Lu P, Nocedal J. L-BFGS-B: FORTRAN subroutines for large scale bound constrained optimization. Tech. Report, NAM-11, EECS Department, Northwestern University, 1994.
- [22] Zhu C, Byrd RH, Lu P, Nocedal J. L-BFGS-B: a limited memory FORTRAN code for solving bound constrained optimization problems Tech. Report, NAM-11, EECS Department, Northwestern University, 1994.
- [23] Mei Y, Wang S, Shen X, Rabke S, Goenezen S. Mechanics based tomography: a preliminary feasibility study. *Sensors* 2017;17(5):1075.